Confined Interlayer Water Promotes Structural Stability for High-Rate Electrochemical Proton Intercalation in Tungsten Oxide Hydrates

James B. Mitchell,[1] Natalie R. Geise,[2,3] Alisa R. Paterson,[1] Naresh C. Osti,[4] Yangyunli Sun,[5] Simon Fleischmann,[1] Rui Zhang,[6] Louis A. Madsen,[6] Michael F. Toney,[3] De-en Jiang,[5] Alexander I. Kolesnikov,[4] Eugene Mamontov,[4] & Veronica Augustyn[1*]

1. *Department of Materials Science and Engineering*, North Carolina State University, Raleigh, NC; USA.
2. *Department of Chemistry,* Stanford University, Stanford, CA; USA.
3. *Stanford Synchrotron Radiation Lightsource,* SLAC National Accelerator Laboratory, Menlo Park, CA; USA.
4. *Neutron Scattering Division,* Oak Ridge National Laboratory, Oak Ridge, TN; USA.
5. *Department of Chemistry*, University of California, Riverside, Riverside, CA; USA.
6. *Department of Chemistry,* Virginia Polytechnic Institute and State University, Blacksburg, VA; USA.

[*]Corresponding author's e-mail: vaugust@ncsu.edu

Abstract

There is widespread interest in determining the structural features of redox-active electrochemical energy storage materials that enable simultaneous high power and high energy density. Here, we present the discovery that confined interlayer water in crystalline tungsten oxide hydrates, $WO_3 \cdot nH_2O$, enables highly reversible proton intercalation at sub-second timescales. By comparing the structural transformation kinetics and confined water dynamics of the hydrates with anhydrous WO_3, we determine that the rapid electrochemical proton intercalation is due to the ability of the confined water layers to isolate structural transformations to two dimensions while stabilizing the structure along the third dimension. As a result, these water layers provide both structural flexibility and stability to accommodate intercalation-driven bonding changes. This provides an alternative explanation for the fast energy storage kinetics of materials that incorporate structural water and provides a new strategy for enabling high power and high energy density with redox-active layered materials containing confined fluids.

TOC Graphic

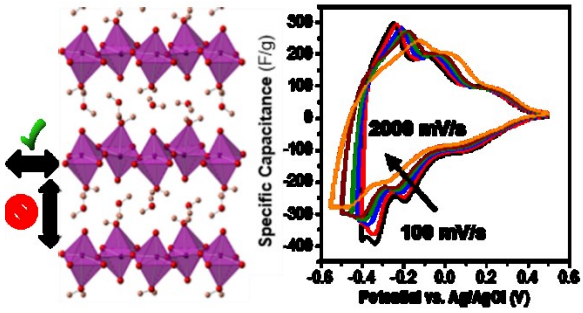

Over the past few decades, the most widely investigated approach to increase the power density of redox-active materials has been nanostructuring to decrease diffusion distances and increase the electrochemical interfacial area.[1–4] While successful in increasing power capability, this design strategy has drawbacks, mainly low volumetric energy density and propensity for parasitic side reactions due to the unconstrained porosity.[5] An emerging strategy is to find structural features that can enable fast ion transport in redox-active materials. In recent years, these include the discovery of intercalation pseudocapacitance via solid-solution intercalation in crystalline Nb_2O_5,[6] the presence of oxygen vacancies in MoO_{3-x},[7] and oxygen intercalation in perovskite oxides like $LaMnO_3$.[8] Another prominent example is the presence of confined fluids such as structural water.[9] Structural water can be found in diverse classes of materials including oxides,[10] chalcogenides,[11] MXenes,[12] and framework materials such as Prussian blue analogs[13–15] and metal organic frameworks.[16] It has been hypothesized that proton transport in materials with extended structural water networks may occur via the Grotthuss mechanism,[13,17] whereby very fast (picosecond timescale) proton transport occurs by hydrogen bonding to adjacent water molecules.[18] However, it is not yet clear whether this mechanism can manifest itself in materials when proton transport is coupled to a faradaic reaction, as in electrochemical energy storage.

In order to understand the role of structural water during proton transport that is coupled to a faradaic reaction, we have been investigating the electrochemical de/intercalation of protons in hydrated tungsten oxides, $WO_3 \cdot nH_2O$ (n = 1, 2), whose structural water content and structure is well-known (**Figure 1**).[19,20] Recently, we found that the presence of structural water leads to a transition in the energy storage mechanism from solid-state diffusion limited in WO_3 to surface-limited (or pseudocapacitive) in $WO_3 \cdot 2H_2O$.[19] We also found that the presence of structural water minimized the electrochemically-driven deformation of $WO_3 \cdot 2H_2O$.[20]

Here, we investigate the role of structural water on the observed kinetic differences between $WO_3 \cdot nH_2O$ and WO_3 by coupling electrochemical characterization with fundamental studies of the structure and dynamics of both the solid-state structure and confined water network. Our measurements reveal that structural water in $WO_3 \cdot nH_2O$ is highly confined, which allows for rapid and facile structural transformation during electrochemical proton intercalation. We demonstrate that the facile structural transformation of $WO_3 \cdot nH_2O$ allows for reversible proton intercalation at a scan rate of 2 V s^{-1}, corresponding to a charge/discharge time of only ~ 500 ms. We hypothesize that the role of the confined water network is to stabilize the layered structure of $WO_3 \cdot nH_2O$ as it undergoes intercalation-induced phase transformations at high rates. This leads us to propose a new materials design strategy for high power, high energy density storage via the presence of confined fluids. This concept could be extended to other layered materials, such as oxides[10] and chalcogenides[11] via interlayer engineering.

The electrochemical intercalation of protons into $WO_3 \cdot nH_2O$ or anhydrous WO_3 can be expressed as:

$$WO_3 \cdot nH_2O;\ WO_3 + xH^+ + xe^- \leftrightarrow H_xWO_3 \cdot nH_2O;\ H_xWO_3 \quad (0 \leq x \leq 1) \qquad (1)$$

where x is the extent of proton storage, with a maximum of 1.[21] This leads to maximum gravimetric capacities of 360 C g^{-1} for $WO_3 \cdot 2H_2O$, 386 C g^{-1} for $WO_3 \cdot H_2O$, and 416 C g^{-1} for WO_3. Despite the modest gravimetric capacities, these materials serve as model systems for understanding the role of structural water during proton intercalation at fast timescales due to the stoichiometric, well-ordered water network, the fact that the same redox reaction is present in all three phases, and that the dehydration reaction to form each phase does not affect overall particle surface area or morphology.[19]

To probe electrochemical proton intercalation into $WO_3 \cdot nH_2O$ under extremely short timescales (second to sub-second), we electrodeposited $WO_3 \cdot nH_2O$[22] and WO_3 thin film electrodes (~300 nm) and performed cyclic voltammetry with sweep rates (v) from 100 to 2,000 mV s^{-1} (timescales ranging from 9 s to 500 ms) in a sulfuric acid electrolyte. The high rate-electrochemical behavior of all three phases at 2 V s^{-1} (~ 500 ms charge / discharge) is shown in Figure 1d. In line with our previous electrochemical characterization with thicker electrodes made with acid-precipitated particles,[19] the voltammetric response of the two hydrated structures is more reversible than for WO_3. This is indicated by their decreased redox peak separation (**Figure S1**) and rapid turnover from the cathodic to anodic current at the low potential limit of -0.55 V *vs.* Ag/AgCl. The capacity as a function of sweep rate is quantified in Figure 1e (the voltammetric responses associated with these sweep rates are shown in Figure S1; the potential window was expanded at faster sweep rates). At these extremely fast timescales for electrochemical energy storage, $WO_3 \cdot nH_2O$ stores more protons than WO_3. It is important to note that according to our prior study,[19] the capacity of WO_3 is initially higher than $WO_3 \cdot nH_2O$ but decays rapidly with increasing rates. For $WO_3 \cdot 2H_2O$ and $WO_3 \cdot H_2O$, the similarities of the voltammetry and capacity retention indicate that the proton storage mechanisms are similar. Both hydrated phases exhibit ~ 90% retention from 100 mV s^{-1} to 2 V s^{-1}, while that of the anhydrous phase is only 60%. To investigate the role of structural water in the observed kinetic differences, the electrochemically-driven structural transformations of $WO_3 \cdot 2H_2O$ and WO_3 were investigated with *operando* X-ray diffraction (XRD).

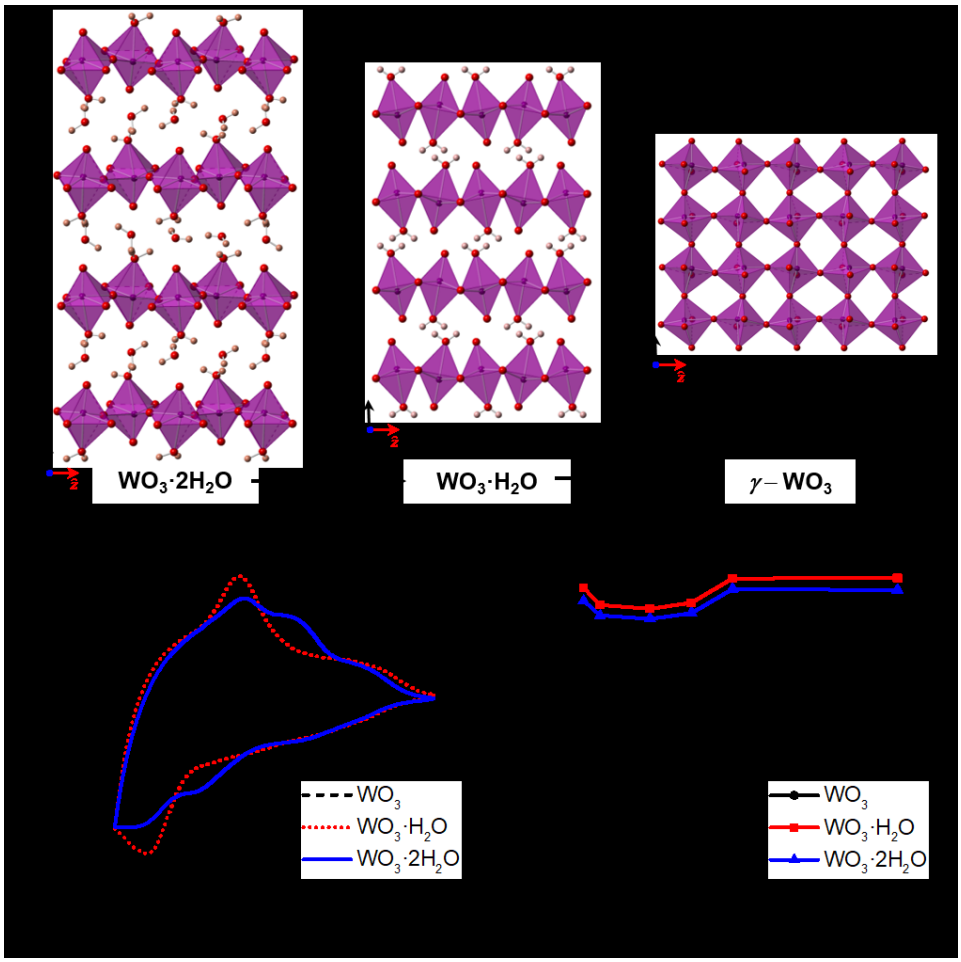

Figure 1 | Crystal Structures and Electrochemical Proton Intercalation at Second and Sub-Second Timescales. Crystal structures of (a) monoclinic $WO_3 \cdot 2H_2O$, (b) orthorhombic $WO_3 \cdot H_2O$, and (c) monoclinic γ-WO_3. $WO_3 \cdot 2H_2O$ exists as layers of corner-sharing $WO_5(OH_2)$ octahedra separated by an additional water layer bound inside the crystal lattice through hydrogen bonding. Dehydrating at 120 °C yields $WO_3 \cdot H_2O$ with a layered structure of corner-sharing $WO_5(OH_2)$ octahedra without interlayer lattice water. Heating at temperatures above 350 °C yields the anhydrous WO_3 which exhibits a distorted ReO_3-type structure of corner-sharing octahedra. (d) Electrochemical proton intercalation of each phase in 0.5 M H_2SO_4 at 2 V s^{-1}. (e) Specific capacity versus sweep rate shows the improved capacity retention of the layered, hydrated structures at

second and sub-second timescales. The increase in capacity at higher scan rates is a result of the increased potential window (see Figure S1).

Faradaic electrochemical energy storage inevitably leads to structural changes that may be accompanied with phase transitions.[23,24] These structural transformations are often the rate-limiting steps for electrochemical energy storage with intercalation-based materials.[25,26] In order to probe the electrochemically-induced structural transformations of $WO_3 \cdot 2H_2O$ and WO_3, we performed *operando* synchrotron XRD at different cyclic voltammetry sweep rates. Of the two hydrated phases, only the $WO_3 \cdot 2H_2O$ was characterized due to the similarity of their electrochemical responses. Here, we utilized higher mass loading slurry-type electrodes made from acid-precipitated particles to ensure sufficient signal from the XRD experiment. **Figure S2** is a schematic of the *in situ* electrochemical cell used in these experiments, and representative cyclic voltammograms (CVs) of $WO_3 \cdot 2H_2O$ and WO_3 in the custom cell are shown in **Figure S3**.

Figure 2 shows the one-dimensional diffraction patterns of $WO_3 \cdot 2H_2O$ and WO_3 as a function of time and potential at sweep rates of 1 and 100 mV s^{-1}. As observed in our previous *ex situ* XRD experiments,[20] the layered, hydrated structure undergoes a reversible phase transition with electrochemical proton de/intercalation. This is indicated by the reversible merging of the two sets of peaks at ~ 13.5° and 15.5° 2θ when the extent of proton intercalation in $H_xWO_3 \cdot 2H_2O$ is ~ 0.04, which is concomitant with the cathodic / anodic redox peaks at ~ 0 V vs. Ag/AgCl (Figure 2a). The progression of this structural transformation is highlighted in the one-dimensional diffraction patterns extracted from the *operando* measurements (**Figure S4)**. The peak merging is attributed to lattice distortions within the two-dimensional $WO_5(OH_2)$ layers toward a more symmetric orthorhombic structure.[27,28] The transformation begins with $x \sim 0.02$ and is practically

complete at $x \sim 0.04$ (Figure S4b), which corresponds to a full transformation in just 40 s. Interestingly, we find that the (010) peak at ~ 7.5°, signifying the interlayer spacing (6.96 Å), does not shift or change intensity with proton de/intercalation. When the sweep rate is increased to 100 mV s^{-1} (charge / discharge times < 10 sec), the reversible phase transition is still present with a faster transformation time of just 7 s (Figure 2c), and the interlayer spacing remains constant.

These results are significant because the intercalation pseudocapacitive charge storage has been previously hypothesized to only occur in materials that do not undergo phase transformations.[29] We hypothesize that the stability of the interlayer indicates that the confined water molecules isolate the electrochemically-driven structural transformations to two dimensions within the $WO_5(OH_2)$ octahedral network, leading to facile ion transport within the structure. To determine whether similar structural stability is present in $WO_3 \cdot H_2O$, we performed *ex situ* XRD of $H_{0.1}WO_3 \cdot H_2O$ (**Figure S5**) and observed a slight decrease in the interlayer spacing, ~ 0.6 %. This is commensurate with the interlayer spacing change for proton intercalation into the well-known pseudocapacitive oxide, birnessite $MnO_2 \cdot nH_2O$ (~ 1 % per 0.1 mol of e^-)[30] and again highlights the stability of the structural water network in $WO_3 \cdot nH_2O$.

The kinetics of the structural response in WO_3 are drastically different as compared to $WO_3 \cdot 2H_2O$ (Figure 2b). The onset of the structural transformation still occurs with intercalation of ~ 0.02 protons and at the cathodic redox peak (Figure S4d), as with $WO_3 \cdot 2H_2O$. However, even at a proton content of $x \sim 0.07$, the structural transformation to the protonated tetragonal structure of H_xWO_3[31–33] is incomplete even after 240 s. The extended two-phase region between γ-WO_3 and tetragonal H_xWO_3 indicates sluggish phase transformation kinetics in the absence of a confined interlayer water network. This is likely the rate-limiting process that prevents fast transport of protons through the anhydrous material. The inability of the WO_3 structure to respond to

electrochemical proton intercalation at fast rates is especially evident by the lack of structural transformation at 100 mV s^{-1} (Figure 2d). The structure is in effect "frozen" at these faster charge / discharge times (t < 10 s) and unable to rapidly accommodate protons.

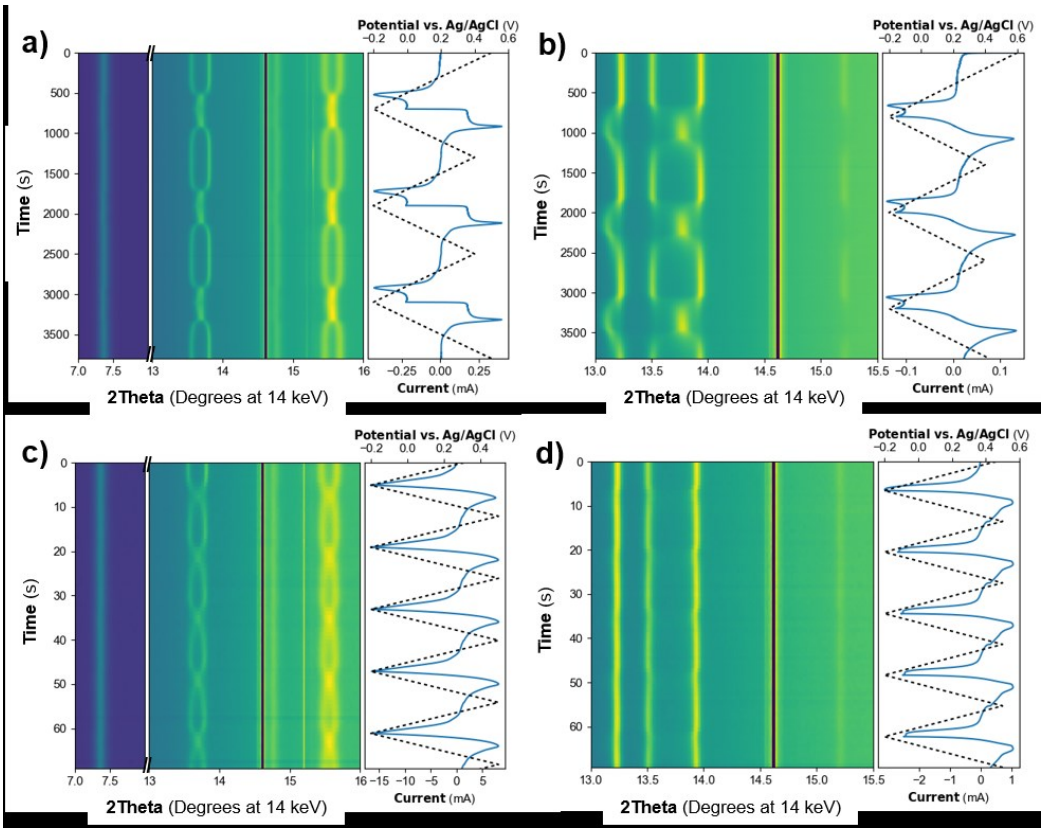

Figure 2 | *Operando* XRD of Electrochemically-Induced Phase Transformations in $WO_3 \cdot 2H_2O$ and WO_3. Synchrotron XRD color maps of $WO_3 \cdot 2H_2O$ (a, c) and WO_3 (b, d) as a function of electrochemical cycling at 1 (a, b) and 100 (c, d) mV s^{-1}. The black line at ~ 14.5° 2θ indicates an edge in the area detector. The applied potential as a function of time is depicted by the black dashed lines at the right of each plot, and the resulting current is shown by the blue solid curves. The highly reversible phase transition of $WO_3 \cdot 2H_2O$ can be observed at both 1 and 100 mV s^{-1} by the reversible merging of the (200) / (001) and (101) / (011) diffraction peaks at ~ 13.5° and 15.5°, respectively. The interlayer spacing, indicated by the (010) diffraction peak at ~ 7.5°, is

immobile during electrochemical proton de/intercalation. The reversible phase transition of WO_3 is shown by the reversible merging / shifting of the (002), (020), and (200) diffraction peaks found at $2\theta \sim 13.25°$, 13.5°, and 14°, respectively. However, the anhydrous structure is practically "frozen" at 100 mV s^{-1}.

To elucidate the role of structural water in enabling sub-second electrochemical proton intercalation into $WO_3 \cdot nH_2O$, we characterized the physical structure and dynamics of the structural water in the acid-precipitated powders using neutron scattering and solid-state nuclear magnetic resonance (SSNMR). **Figure 3a** shows the elastic neutron scattering intensity of each phase integrated from scattering vector (Q) = 0.5 – 1.7 $Å^{-1}$ as a function of temperature; the overall increase in elastic intensity scales appropriately with the amount of structural water in each phase. All plots exhibit a small deviation from the linear decrease with temperature, indicative of the presence of small amounts of residual surface moisture in the samples (several percent of total water by SSNMR). We used a two-component model to fit the QENS spectra of the hydrated phases; the resulting signal widths are presented in Figure 3b, c. The figure reveals the presence of two different types of water populations in the hydrated materials: one with quicker motion (broad component) and another with relatively slower motion (narrow component). Additionally, the half-width-half-max (HWHMs) of the quasielastic signals are largely independent of both temperature and Q for both hydrated phases, indicating the presence of only localized, and not translational, motion of water molecules up to nanosecond timescales. Any translational motion of water molecules on the ps to ns timescale would manifest itself in the QENS signal width increasing with Q. Therefore, the water in $WO_3 \cdot nH_2O$ is highly confined, with only some local conformational, but not translational, freedom.

We further investigated the structural water in $WO_3 \cdot nH_2O$ with ^1H SSNMR spectroscopy measurements (Figure 3d), which carry implications for motions on microsecond or faster timescales. All three phases exhibit a sharp peak at ~ 0 ppm likely due to fast moving surface-adsorbed water as powdered samples contain significant particle surface area. The $WO_3 \cdot nH_2O$ phases exhibit a broad doublet with a spectral splitting of ~ 70 ppm. This appears to be a "Pake" doublet (a superposition of spectra of randomly ordered crystallites), which is commonly observed in the ^1H NMR spectra of crystal hydrates.[34] We estimate that the rate of exchange of water protons between different water sites in the hydrated WO_3 samples occurs substantially more slowly than the inverse of the full width of the Pake powder spectrum (~ 140 ppm = 80 kHz, or ~ 10 μs timescale). The presence of this slow-moving structural feature that leads to the Pake spectral pattern is in agreement with the QENS results that there is no significant translational motion of water in $WO_3 \cdot nH_2O$ on a timescale relevant to liquid-like water diffusion, such as that observed in polymeric ion conductors with nm-scale confinement of water.[35] In other words, the structural water is translationally immobile on timescales from ps to μs and thus is well confined. It is worth noting that the lack of translational mobility of confined structural water was also observed in the isostructural $MoO_3 \cdot nH_2O$ with solid-state ^1H NMR.[36]

The vibrational dynamics of each phase were investigated using inelastic neutron scattering (INS, Figure 3e, f). Distinct differences are observed in the vibrational spectra of all three phases. The neutron scattering cross-section of hydrogen is ~ 20 times larger than that of tungsten and oxygen. Therefore, the INS spectrum of WO_3 has negligible intensity as compared to $WO_3 \cdot nH_2O$, and only extends until ~ 115 meV. The layered, hydrated structures of $WO_3 \cdot H_2O$ and $WO_3 \cdot 2H_2O$ exhibit appreciable density of states up to higher frequencies due to the presence of structural water molecules. The O-H symmetric and antisymmetric stretching modes are observed as a peak at ~

428 meV for $WO_3 \cdot H_2O$, and as three peaks at 395, 420, and 441 meV for $WO_3 \cdot 2H_2O$ (due to two types of structural water). The intramolecular H-O-H bending mode is at ~ 200 meV, and the peak is ~ 2 times broader for $WO_3 \cdot 2H_2O$. The spectrum of ice – I_h is shown to highlight the similarities between crystalline water and the confined water network present in the $WO_3 \cdot nH_2O$. Ice exhibits similar O-H stretching behavior to $WO_3 \cdot H_2O$ but has broadened peaks at lower frequencies due to hydrogen disorder in the hexagonal lattice. Overall, we find that the structural water layers are well-ordered and quite translationally immobile on the ps to μs timescales. We hypothesize that the presence of these confined water networks in the interlayer of $WO_3 \cdot 2H_2O$ enables the facile, basically 2D, phase transformation observed during electrochemical proton intercalation by effectively stabilizing the interlayer and restricting structural changes to two dimensions.

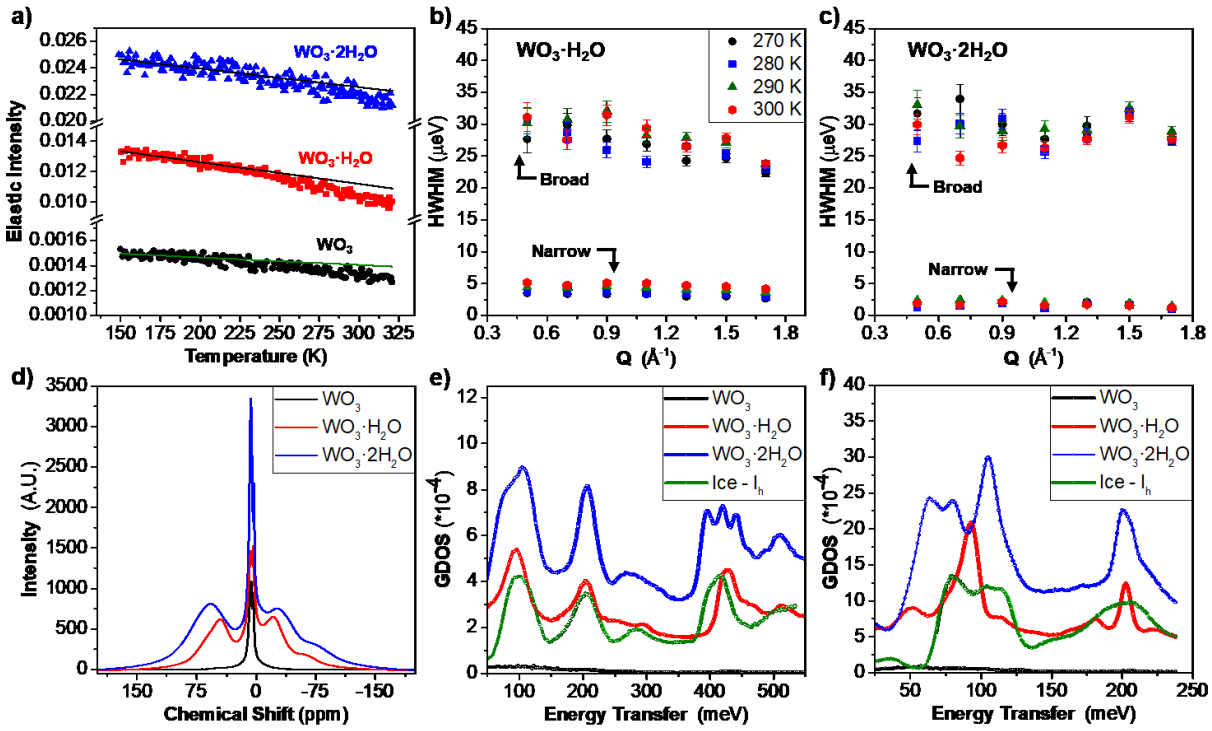

Figure 3 | Characterization of the Structural Water Dynamics in $WO_3 \cdot nH_2O$. (a) Elastic neutron scattering intensity of pristine $WO_3 \cdot nH_2O$ and WO_3 powders as a function of temperature.

Linear trends were extrapolated from data points within the low-temperature region (150 K – 200 K). Half-width-half-max (HWHM) of the wide and narrow components of the quasielastic fits exhibit very little temperature and Q dependence for both (b) $WO_3 \cdot H_2O$ and (c) $WO_3 \cdot 2H_2O$. (d) Solid-state ^1H NMR spectra of $WO_3 \cdot nH_2O$ and WO_3 (static samples), demonstrating relatively slow exchange dynamics (~ 10 μs timescale or slower) for interlayer confined water. Generalized vibrational density of states (GDOS) of $WO_3 \cdot nH_2O$ from INS at T = 5 K with E_i = (e) 600 and (f) 250 meV. Ice – I_h is included to compare crystalline water to the confined water networks in $WO_3 \cdot nH_2O$.

Neutron scattering and SSNMR of the pristine $WO_3 \cdot nH_2O$ indicate that the structural water is a highly confined, well-ordered network. To investigate whether the same is true of the electrochemically protonated phases, we performed *ex situ* neutron scattering on electrochemically protonated electrodes of $H_{0.13}WO_3 \cdot H_2O$ and $H_{0.1}WO_3$. Here, we studied $WO_3 \cdot H_2O$ because $WO_3 \cdot 2H_2O$ undergoes dehydration of its hydrogen-bonded interlayer water in the conditions necessary for *ex situ* neutron scattering sample preparation (see Methods for details).[37] The *ex situ* QENS shows that there is increased elastic intensity (near zero energy transfer) in the $H_{0.13}WO_3 \cdot H_2O$ charged electrode, commensurate with the expected increase of protons (**Figure 4a**). Importantly, the quasielastic scattering "wings" signal of the pristine and charged electrodes are similar, indicating similar dynamics of the structural water network before and after electrochemical proton intercalation. That is, irrespective of the electrode charge state, the intercalated protons are static on the timescale probed by QENS and do not affect the highly localized motion of the structural water molecules. The increase in elastic intensity and lack of change in quasielastic scattering signal is also observed when comparing charged $H_{0.1}WO_3$ with

pristine WO_3 (**Figure S6).** The static nature of the intercalated protons on the pico- to nanosecond timescales probed with QENS suggests that the confined water network of $WO_3 \cdot nH_2O$ does not enable either translational or correlated hopping of protons. This hypothesis is in agreement with the lack of interlayer spacing change in the *operando* XRD of $WO_3 \cdot 2H_2O$ and the storage of protons in a bridging oxygen site from *ex situ* INS and *ab initio* molecular dynamics (AIMD) simulations, *vide infra*.

Ex situ INS was utilized to determine the intercalated proton binding site in $H_{0.13}WO_3 \cdot H_2O$. The intercalated protons lead to the presence of a new peak at ~ 150 meV and a shift in the O-H stretching mode peak to ~ 420 meV, as compared to the pristine electrode (Figure 4b, c). Both the total and projected vibrational densities of states (VDOS) from the AIMD of the protonated $WO_3 \cdot H_2O$ reveal that the peak at ~ 150 meV is consistent with the W-O-H bending mode of a proton present at the bridging oxygen (O_b) site (Figure 4d and **Figure S7)** although the storage of protons at a terminal oxygen is also possible (O_t)**.** DFT calculations of $H_{0.13}WO_3 \cdot 2H_2O$ indicate that intercalated protons prefer only the O_b sites (**Figure S8**), which is in line with the lack of interlayer spacing change observed from *operando* XRD. These proton site preferences are in agreement with prior DFT calculations on $H_xWO_3 \cdot nH_2O$,[38] which also indicate a rotationally enabled proton transport mechanism that may be active in the present materials. The location of the intercalated proton in $H_{0.1}WO_3$ in the bridging site is already well-known,[39] and our INS and density functional theory (DFT) results are in line with these prior observations (**Figure S9**). The *ex situ* INS and DFT results indicate that $WO_3 \cdot nH_2O$ and WO_3 store protons at bridging oxygen sites, and thus we hypothesize that the significant differences in electrochemical proton intercalation kinetics are attributed to differences in the ability of the respective solid state structures to undergo necessary structural transformations.

Lastly, it has been proposed that a low activation energy barrier determined from impedance spectroscopy could be utilized to determine the presence of Grotthuss transport in solid-state energy storage materials. We found that the activation energy barrier for a $WO_3 \cdot 2H_2O$ pellet under such conditions does give a low value of 0.2 eV (**Figure S10**). However, the dependence of this value on the ambient humidity (**Figure S11**) as well as prior impedance results with $WO_3 \cdot nH_2O$[40] and metal organic frameworks[41] indicate that such a low activation energy is indicative of the motion of surface-adsorbed water, whose contribution is significant in cold-pressed pellets made from powdered materials. This is in-line with our SSNMR results of the pristine materials that indicate the presence of fast-moving water on the surface of particles. As a result, we hypothesize that the confined water in $WO_3 \cdot nH_2O$ plays a critical role in enabling facile structural transformations in only two dimensions.

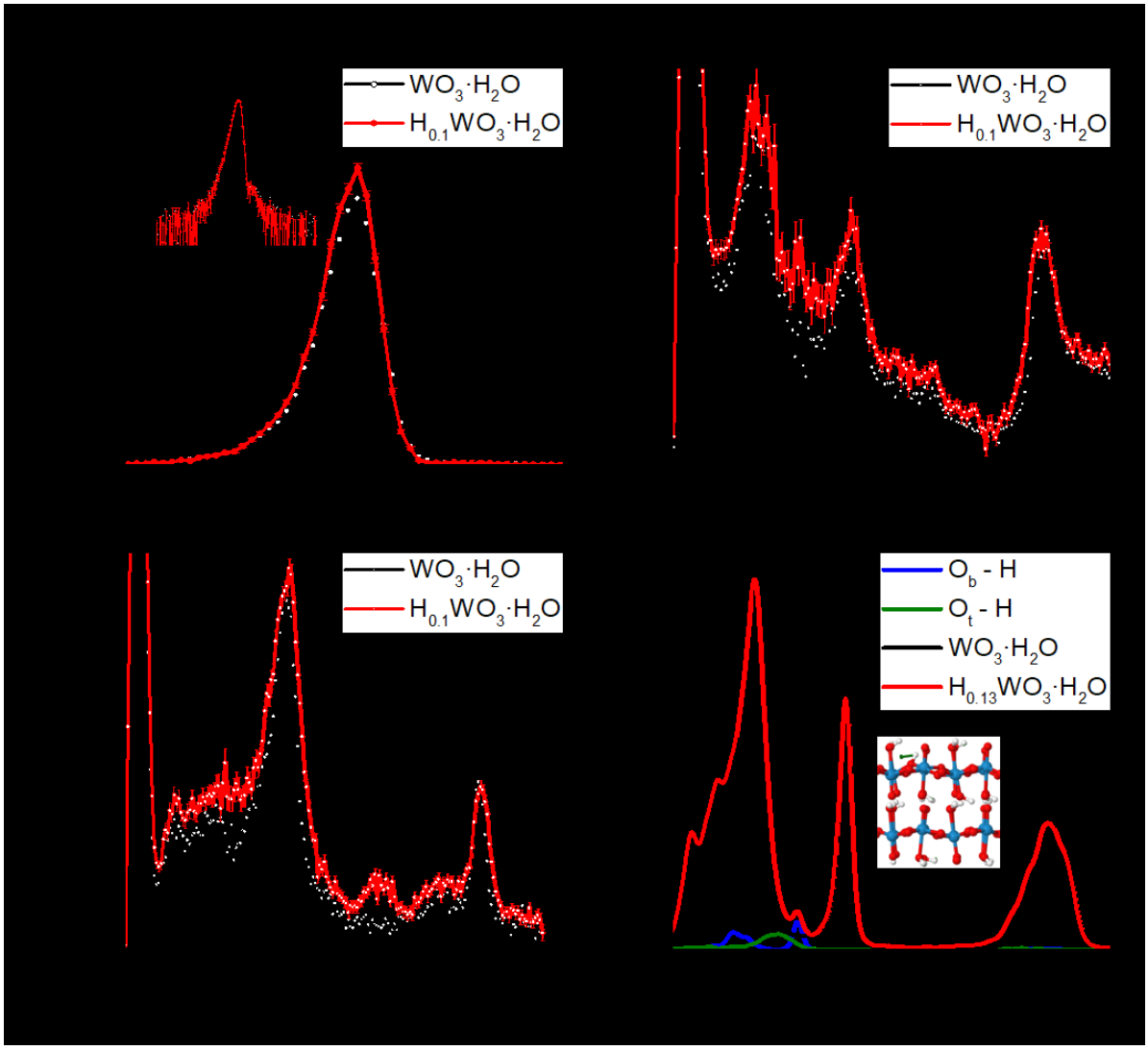

Figure 4 | Proton Intercalation Site in $WO_3 \cdot nH_2O$. (a) *Ex situ* QENS of an $WO_3 \cdot H_2O$ electrode in the pristine ($WO_3 \cdot H_2O$, *black*) and intercalated ($H_{0.1}WO_3 \cdot H_2O$, *red*) states at T = 300 K and Q = 0.9 $Å^{-1}$ (the asymmetry of the elastic peak is due to the intrinsically asymmetric resolution function often characteristic of spallation-source based neutron spectrometers). The intensity is plotted in logarithmic scale in the inset to highlight the quasielastic scattering "wings" signal. *Ex situ* INS of the same electrodes at T = 5 K with incident energies E_i = (b) 600 and (c) 250 meV. Generalized vibrational density of states (GDOS) versus energy transfer depicts the vibrational modes of protons in $WO_3 \cdot H_2O$. *Ab initio* molecular dynamics simulations of the vibrational

density of states (VDOS, (d)) show the effect of protons at the terminal (O_t, *green*) and bridging (O_b, *blue*) oxygen atoms to the overall spectrum.

Here, we present the unexpected discovery of the role of structural water in crystalline transition metal oxide hydrates in enabling both structural flexibility and stability for highly reversible, sub-second electrochemical intercalation. The confined and ordered nature of the structural water, as probed with neutron scattering and SSNMR, coupled with *operando* XRD results, demonstrate the ability for $WO_3 \cdot nH_2O$ to undergo extremely facile phase transformations while allowing little-to-no changes in the interlayer spacing. The results presented here indicate that the confined water networks in crystalline hydrates such as $WO_3 \cdot nH_2O$ isolate the structural transformations to two dimensions, leading to more facile electrochemically-driven structural transformations. We hypothesize that this is the mechanism behind the exceptional, sub-second proton intercalation ability of $WO_3 \cdot nH_2O$, and highlights the importance of electrochemically-driven phase transformations in determining kinetic limitations in energy storage intercalation reactions. They also point to the possibility of tuning solid-state structures to minimize electrochemically-driven structural distortions via the incorporation of confined fluids such as structural water, thus introducing a new materials design strategy for fast, pseudocapacitive energy storage.

Supporting Information Available: Experimental Methods, Electrochemical Characterization of $WO_3 \cdot nH_2O$, Schematic of *in situ* Cell, Electrochemistry of *in situ* XRD Samples, Electrochemically Induced Phase Transitions of Tungsten Oxide, *Ex Situ* XRD of $WO_3 \cdot H_2O$, *Ex Situ* QENS of WO_3, Proton Storage Sites in $H_x\ WO_3 \cdot nH_2O$ ($n = 0,1,2$), Conductivity of $WO_3 \cdot 2H_2O$, SEM of γ-WO_3, Raman Spectra of Electrodeposited Films, Electrochemical Characterization of *ex situ* Neutron Scattering Samples, Table of Compositions for *ex situ* Neutron Scattering Samples.

Acknowledgements

We thank Nikki Creange, John McGarrahan, Carolyn Grimley, and Prof. Elizabeth Dickey for assistance with pellet pressing and the temperature-controlled stage for impedance measurements. We also thank Michael Spencer for performing scanning electron microscopy. J.B.M., A.R.P., and V.A. acknowledge support from the National Science Foundation under Grant No. 1653827 for material synthesis, electrochemical characterization, and XRD. N.C.O., Y.S., D.J., A.I.K., and E.M. acknowledge funding from the Fluid Interface Reactions, Structures and Transport (FIRST) Center, an Energy Frontier Research Center funded by the U.S. Department of Energy, Office of Science, Office of Basic Energy Sciences for neutron scattering and computation. N.R.G. was supported by the Department of Defense (DoD) through the National Defense Science & Engineering Graduate Fellowship (NDSEG) Program. R.Z. and L.A.M. acknowledge funding from the National Science Foundation under award DMR 1810194 for SSNMR. Use of the Stanford Synchrotron Radiation Lightsource, SLAC National Accelerator Laboratory, is supported by the U.S. Department of Energy, Office of Science, Office of Basic Energy Sciences under Contract No. DE-AC02-76SF00515. A portion of this research used resources at the Spallation Neutron Source, a DOE Office of Science User Facility operated by the

Oak Ridge National Laboratory. Oak Ridge National Laboratory is managed by UT-Battelle, LLC, for U.S. DOE under Contract No. DEAC05-00OR22725. SEM and *ex situ* XRD was performed at the Analytical Instrumentation Facility (AIF) at North Carolina State University (NCSU), which is supported by the State of North Carolina and the National Science Foundation (Grant ECCS-1542015). The AIF is a member of the North Carolina Research Triangle Nanotechnology Network (RTNN), a site in the National Nanotechnology Coordinated Infrastructure (NNCI).

References

1. Bruce, P. G., Scrosati, B. & Tarascon, J.-M. Nanomaterials for rechargeable lithium batteries. *Angew. Chem. Int. Ed. Engl.* **47**, 2930–2946 (2008).
2. Aricò, A. S., Bruce, P., Scrosati, B., Tarascon, J.-M. & van Schalkwijk, W. Nanostructured materials for advanced energy conversion and storage devices. *Nat. Mater.* **4**, 366–77 (2005).
3. Manthiram, A., Vadivel Murugan, A., Sarkar, A. & Muraliganth, T. Nanostructured electrode materials for electrochemical energy storage and conversion. *Energy Environ. Sci.* **1**, 621–638 (2008).
4. Rauda, I. E., Augustyn, V., Dunn, B. & Tolbert, S. H. Enhancing Pseudocapacitive Charge Storage in Polymer Templated Mesoporous Materials. *Acc. Chem. Res.* **46**, 1113–1124 (2013).
5. Palacín, M. R., Simon, P. & Tarascon, J. M. Nanomaterials for Electrochemical Energy Storage : the Good and the Bad. *Acta Chim. Slov.* **63**, 417–423 (2016).
6. Augustyn, V. *et al.* High-rate electrochemical energy storage through Li+ intercalation pseudocapacitance. *Nat. Mater.* **12**, 518 (2013).
7. Kim, H.-S. *et al.* Oxygen vacancies enhance pseudocapacitive charge storage properties of MoO_{3-x}. *Nat. Mater.* **16**, 454 (2016).
8. Mefford, J. T., Hardin, W. G., Dai, S., Johnston, K. P. & Stevenson, K. J. Anion charge storage through oxygen intercalation in $LaMnO_3$ perovskite pseudocapacitor electrodes. *Nat. Mater.* **13**, 726–32 (2014).
9. Augustyn, V. & Gogotsi, Y. 2D Materials with Nanoconfined Fluids for Electrochemical Energy Storage. *Joule* **1**, 443–452 (2017).

10. Bunker, B. C. & Casey, W. H. *The Aqueous Chemistry of Oxides*. New York (Oxford University Press, 2016).

11. Schollhorn, R. *Intercalation Chemistry*. New York (eds. Whittingham, M. S. & Jacobson, A. J.) (Academic Press, 1982).

12. Lukatskaya, M. R. *et al.* Ultra-high-rate pseudocapacitive energy storage in two-dimensional transition metal carbides. *Nat. Energy* **2**, 17105 (2017).

13. Wu, X. *et al.* Diffusion-free Grotthuss topochemistry for high-rate and long-life proton batteries. *Nat. Energy 2019* **4**, 123–130 (2019).

14. Pasta, M. *et al.* Full open-framework batteries for stationary energy storage. *Nat. Commun.* **5**, 3007 (2014).

15. Mizuno, Y. *et al.* Suppressed Activation Energy for Interfacial Charge Transfer of a Prussian Blue Analog Thin Film Electrode with Hydrated Ions (Li^+, Na^+, and Mg^{2+}). *J. Phys. Chem. C* **117**, 10877–10882 (2013).

16. Hmadeh, M. *et al.* New Porous Crystals of Extended Metal-Catecholates. *Chem. Mater.* **24**, 3511–3513 (2012).

17. Whittingham, M. S. Hydrogen motion in oxides: from insulators to bronzes. *Solid State Ionics* **168**, 255–263 (2004).

18. Marx, D. Proton Transfer 200 Years after von Grotthuss : Insights from Ab Initio Simulations. *Chemphyschem* **7**, 1848–1870 (2006).

19. Mitchell, J. B., Lo, W. C., Genc, A., LeBeau, J. & Augustyn, V. Transition from Battery to Pseudocapacitor Behavior via Structural Water in Tungsten Oxide. *Chem. Mater.* **29**, 3928–3937 (2017).

20. Wang, R. *et al.* Operando Atomic Force Microscopy Reveals Mechanics of Structural

Water Driven Battery-to-Pseudocapacitor Transition. *ACS Nano* **12**, 6032–6039 (2018).

21. Granqvist, C. G. *Handbook of inorganic electrochromic materials*. Amsterdam (Elsevier, 1995).

22. Pugolovkin, L. V *et al.* Electrodeposited non-stoichiometric tungstic acid for electrochromic applications: film growth modes, crystal structure, redox behavior and stability. *Appl. Surf. Sci.* **388**, 786–793 (2016).

23. Meethong, N. *et al.* Electrochemically Induced Phase Transformation in Nanoscale Olivines $Li_{1-x}MPO4$ (M = Fe, Mn). *Chem. Mater.* **20**, 6189–6198 (2008).

24. Alfaruqi, M. H. *et al.* Electrochemically Induced Structural Transformation in a γ-MnO_2 Cathode of a High Capacity Zinc-Ion Battery System. *Chem. Mater.* **27**, 3609–3620 (2015).

25. Vassiliev, S. Y., Levin, E. E. & Nikitina, V. A. Kinetic analysis of lithium intercalating systems: cyclic voltammetry. *Electrochim. Acta* **190**, 1087–1099 (2016).

26. Singh, G. K., Ceder, G. & Bazant, M. Z. Intercalation dynamics in rechargeable battery materials: General theory and phase-transformation waves in $LiFePO_4$. *Electrochim. Acta* **53**, 7599–7613 (2008).

27. Dickens, P. G., Kay, S. A., Crouch-Baker, S. & Claridge, D. A. Thermochemistry of the hydrogen insertion compounds formed by the molybdic and tungstic acids $H_xMO_3 \cdot nH_2O$ (M=Mo, n=1; M=W, n=1,2). *Solid State Ionics* **23**, 9–14 (1987).

28. Granqvist, C. G. Electrochromic tungsten oxide films: Review of progress 1993–1998. *Sol. Energy Mater. Sol. Cells* **60**, 201–262 (2000).

29. Augustyn, V., Simon, P. & Dunn, B. Pseudocapacitive oxide materials for high-rate electrochemical energy storage. *Energy Environ. Sci.* **7**, 1597–1614 (2014).

30. Kuo, S.-L. & Wu, N.-L. Investigation of Pseudocapacitive Charge-Storage Reaction of $MnO_2 \cdot nH_2O$ Supercapacitors in Aqueous Electrolytes. *J. Electrochem. Soc.* **153**, A1317 (2006).

31. Strømme Mattsson, M. Cation intercalation in sputter-deposited W oxide films. *Phys. Rev. B* **58**, 11015–11022 (1998).

32. Zhong, Q., Dahn, J. R. & Colbow, K. Lithium intercalation into WO_3 and the phase diagram of Li_xWO_3. *Phys. Rev. B* **46**, 2554–2560 (1992).

33. Ampe, B., Leroy, J. M., Thomas, D. & Tridot, G. Contribution to Study of Systems Tungsten-Oxygen and Tungsten-Vanadium-Oxygen. *Rev. Chim. Miner.* **5**, 801 (1968).

34. Pake, G. E. Nuclear resonance absorption in hydrated crystals: fine structure of the proton line. *J. Chem. Phys.* **16**, 327–336 (1948).

35. Li, J., Park, J. K., Moore, R. B. & Madsen, L. A. Linear coupling of alignment with transport in a polymer electrolyte membrane. *Nat. Mater.* **10**, 507 (2011).

36. Jarman, R. H., Dickens, P. G. & Slade, R. C. T. NMR study of water reorientation in molybdic acids: $MoO_3 \cdot 2H_2O$ and yellow $MoO_3 \cdot H_2O$. *J. Solid State Chem.* **39**, 387–394 (1981).

37. Wang, R., Chung, C.-C., Liu, Y., Jones, J. L. & Augustyn, V. Electrochemical Intercalation of Mg^{2+} into Anhydrous and Hydrated Crystalline Tungsten Oxides. *Langmuir* **33**, 9314–9323 (2017).

38. Lin, H., Zhou, F., Liu, C.-P. & Ozolins, V. Non-Grotthuss proton diffusion mechanism in tungsten oxide dihydrate from first-principles calculations. *J. Mater. Chem. A* **2**, 12280–12288 (2014).

39. Dickens, P. G. & Whittingham, M. S. The Tungsten Bronzes and Related Compounds.

Chem. Soc. Rev. **22**, 30–44 (1968).

40. Li, Y. M., Hibino, M., Miyayania, M. & Kudo, T. Proton conductivity of tungsten trioxide hydrates at intermediate temperature. *Solid State Ionics* **134**, 271–279 (2000).

41. Tominaka, S. & Cheetham, A. K. Intrinsic and extrinsic proton conductivity in metal-organic frameworks. *RSC Adv.* **4**, 54382–54387 (2014).